Table 2. EDXS analysis of Gd- and Dy-CNCs after heated 450°C shown in Figure 4 (at%)

Elements analyzed point	Gd	Dy	C	O
1	7.0	—	92.4	0.6
2	10.6	—	66.1	23.3
3	—	76.9	20.9	2.2
4	—	27.5	51.9	20.6

encapsulated elements are isolated from the outside. Oxidation of encapsulated rare earth elements indicates damage to the graphene capsules and loss of their airtightness. Therefore, MECNCs heated at higher than 400°C in air lose their chemical stability, and the encapsulated elements become erosive. In other words, MECNCs are stable at lower than 350°C and the erosion of encapsulated elements is negligible. This feature is important for biomedical application as the authors have reported the low cytotoxicity of Ce-CNCs (13). In this study, various rare earth elements were encapsulated in carbon nanocapsules. Gd-CNCs had the highest purity (35 wt%) among the synthesized MECNCs and slightly better stability for heating in air up to 450°C. Concerning the Gd-CNCs, paramagnetic properties and magnetic separation were suggested (15, 16). Thus, Gd-CNCs would be favorable for biomedical and other applications.

ACKNOWLEDGMENTS

This work was supported by Research on Advanced Medical Technology in Health and Labour Sciences Research Grants from the Ministry of Health, Labour and Welfare of Japan. A part of this study was also supported by Grant-in-Aid for Scientific Research (B) No.18390509 from the Ministry of Education, Culture, Sports, Science and Technology, Japan.

REFERENCES

1. Ruoff, R.S., Lorents, D.C., Chan, B., Malhotra, R., and Subramoney, S. (1993) Single crystal metals encapsulated in carbon nanoparticles. *Science*, 259: 346.
2. Tomita, M., Saito, Y., and Hayashi, T. (1993) LaC_2 encapsulated in graphite nanoparticles. *Jpn J. Appl. Phys.*, 32: L280.
3. Yosida, Y. (1993) Synthesis of CeC_2 crystals encapsulated within gigantic super fullerenes. *Appl. Phys. Lett.*, 62: 3447.
4. Saito, Y., Yoshikawa, T., Okuda, M., Ohkohchi, M., Ando, Y., Kasuya, A., and Nishina, Y. (1993) Synthesis and electron-beam incision of carbon nanocapsules encaging YC_2. *Chem. Phys. Lett.*, 209: 72.

5. Seraphin, S., Zhou, D., Jiao, J., Withers, J.C., and Loutfy, R. (1993) Selective encapsulation of the carbides of yttrium and titanium into carbon nanoclusters. *Appl. Phys. Lett.*, 63: 2073.
6. Saito, Y., Okuda, M., Yoshikawa, T., Bandow, S., Yamamuro, S., Wakoh, K., Sumiyama, K., and Suzuki, K. (1994) Synthesis of $Sc_{15}C_{19}$ crystallites encapsulated in carbon nanocapsules by arc evaporation of Sc-C composite. *Jpn. J. Appl Phys.*, 33: L186.
7. Funasaka, H., Sugiyama, K., Yamamoto, K., and Takahashi, T. (1995) Synthesis actinide carbides encapsulated within carbon nanoparticles. *J. Appl. Phys.*, 78: 5320.
8. Pasqualini, E., Adelfang, P., and Regueiro, M.N. (1996) Carbon nanoencapsulation of uranium dicarbide. *J. Nucl. Mater.*, 231: 173.
9. Yosida, Y. (1997) A new type of ultrafine particles: rare earth dicarbide crystals encapsulated in carbon nanocages. *Physica*, 229: 301.
10. Sato, Y., Jeyadevan, B., Hatakeyama, R., Kasuya, A., and Tohji, K. (2004) Electronic properties of radial single-walled carbon nanotubes. *Chem. Phys. Lett.*, 385: 323.
11. Mikawa, M., Kato, H., Okumura, M., Narazaki, M., Kanazawa, Y., Miwa, N., and Shinohara, H. (2001) Paramagnetic water-soluble metallofullerenes having the highest relaxivity for MRI contrast agents. *Bioconjugate Chem.*, 12: 510.
12. Bolskar, R.D., Benedetto, A.F., Husebo, L.O., Price, R.E., Jackson, E.F., Wallace, S., Wilson, L.J., and Alford, M. (2003) First soluble $M@C_{60}$ derivatives provide enhanced access to metallofullerenes and permit in vivo evaluation of $Gd@C_{60}[C(COOH)_2]_{10}$ as a MRI contrast agent. *J. Am. Chem. Soc.*, 125: 5471.
13. Uo, M., Tamura, K., Sato, Y., Yokoyama, A., Watari, F., Totsuka, Y., and Tohji, K. (2005) The cytotoxicity of metal-encapsulating carbon nanocapsules. *Small*, 1: 816.
14. Ajayan, P.M., Ebbesen, T.W., Ichihashi, T., Iijima, S., Tanigaki, K., and Hiura, H. (1993) Opening carbon nanotubes with oxygen and implications for filling. *Nature*, 362: 522.
15. Majetich, S.A., Artman, J.O., McHenry, M.E., Nuhfer, N.T., and Staley, S.W. (1993) Preparation and properties of carbon-coated magnetic nanocrystallites. *Phys. Rev. B*, 48: 16845.
16. Subramoney, S., Ruoff, R.S., Lorents, D.C., Chan, B., Malhotra, R., Dyer, M.J., and Parvin, K. (1994) Magnetic separation of GdC_2 encapsulated in carbon nanoparticles. *Carbon*, 32: 507.

Available online at www.sciencedirect.com
SCIENCE DIRECT
Scripta Materialia 54 (2006) 299–303
Scripta MATERIALIA
www.actamat-journals.com

Mechanical properties of binder-free single-walled carbon nanotube solids

Go Yamamoto [a,*], Yoshinori Sato [b], Toru Takahashi [a], Mamoru Omori [a], Akira Okubo [c], Kazuyuki Tohji [b], Toshiyuki Hashida [a]

[a] *Fracture and Reliability Research Institute, Tohoku University, Graduate School of Engineering, 6-6-1 Aza-Aoba, Aramaki, Aobaku, Sendai, Miyagi 980-8579, Japan*
[b] *Graduate School of Environmental Studies, Tohoku University, Sendai 980-8579, Japan*
[c] *Institute for Materials Research, Tohoku University, Sendai 980-8577, Japan*

Received 9 January 2005; received in revised form 8 March 2005; accepted 29 March 2005
Available online 25 October 2005

Abstract

Single-walled carbon nanotubes (SWCNTs) were successfully solidified without any additives using a spark plasma method. Purification of raw soot was crucially important in order to improve the mechanical properties of the SWCNT solid, which exhibited a significant nonlinear deformation response in contrast with brittle fracture of an unpurified SWCNT solid.

Keywords: Single-walled carbon nanotubes; Spark plasma sintering method; Small punch testing method; Mechanical properties; Microstructure

Recent experimental studies have amply demonstrated that individual single-walled carbon nanotubes (SWCNTs) have an extremely high Young's modulus and tensile strength [1,2]. Researchers have mostly examined the possible applications of SWCNTs in polymer [2,3], metal [4] and ceramics [5,6] matrices, and characterized the properties and microstructures of these composite materials. However, the production of SWCNT composites with extremely good mechanical properties is yet to be realized. Additionally, in order to take full advantage of the intrinsic mechanical and physical properties of SWCNTs, it is necessary to produce solid structures that are composed solely of the SWCNTs.

In this work, we have successfully produced binder-free SWCNT disks with purified SWCNTs by using a spark plasma sintering (SPS) method, and the mechanical properties of the disk specimens were investigated by a small punch (SP) testing method. Raw soot synthesized by conventional methods commonly contains metal particles and various forms of carbon [7–9]. Therefore, the effect of the impurities on the mechanical properties and microstructures was investigated by comparing the results obtained from the disk specimens made of the purified SWCNTs and unpurified raw soot.

SWCNTs were synthesized by a direct current arc discharge between a pure graphite cathode and a metal loaded graphite anode. A pure graphite rod (purity 99.9%), 16 mm diameter and 50 mm length, and a 6 mm diameter and 110 mm length graphite rod (99.9%) loaded with Fe and Ni powders (99.99%) were used as cathode and anode, respectively. The arc discharge was carried out under a helium atmosphere of 100 Torr. The discharge current was 70 A, and during the discharge, the gap between the electrodes was maintained at about 3 mm by manually advancing the consumed anode. The raw soot containing SWCNTs

* Corresponding author. Tel.: +81 22 217 7524; fax: +81 22 217 4311.
E-mail address: gyamamoto@rift.mech.tohoku.ac.jp (G. Yamamoto).

1359-6462/$ - see front matter © 2005 Acta Materialia Inc. Published by Elsevier Ltd. All rights reserved.
doi:10.1016/j.scriptamat.2005.03.053

produced by the arc discharge method was retrieved from the upper wall and the roof of the chamber and was homogenized by mixing together regardless of the different sampling locations. In the raw soot, SWCNTs coexist with many by-products such as metal particles, fullerenes, and amorphous carbon [7,10]. Therefore, SWCNTs were separated step by step from the impurities using the following purification process. First, the fullerenes and the amorphous carbon were burned out by heating approximately 600 mg of raw soot at 450 °C and keeping for 30 min in air. Then, the residual soot was heated up to 500 °C and kept for 30 min in air to burn out the graphitic layers surrounding metal particles. Finally, the metal particles were washed out from the soot by treating with 6 M hydrochloric acid solution. The processed soot was filtered and rinsed with deionized water.

Fig. 1(a) and (b) shows the Raman spectra and X-ray diffraction (XRD) profiles of the unpurified raw soot and purified SWCNTs, respectively. Abundance of SWCNTs in the sample is estimated from the intensity ratio I_G/I_D of the Raman spectrum, and is also indicated in Fig. 1(a). It is well known that the Raman intensity ratio I_G/I_D of the peaks at 1350 cm^{-1} (D-band) and 1590 cm^{-1} (G-band) is a good index for the evaluation of the SWCNTs abundance [11,12]. Here, both the samples were measured using 488.0 nm exciting lasers with backscattering configuration. As seen in Fig. 1(a), the I_G/I_D of SWCNTs was about seven times larger than that of raw soot, without any change in each peak position. The XRD profile of the raw soot shows the presence of the C_{60}, graphite and metals. In contrast, the SWCNTs were free of C_{60} and metals, showing only the graphite peak. These results suggest that highly pure SWCNTs have been obtained by the processing conditions used, except for a trace amount of carbon materials other than SWCNTs. The diameter distribution of SWCNTs was determined from the Raman spectra in radial breathing mode (RBM) range [13]. From the peaks at 160 and 180 cm^{-1}, the diameter of the SWCNTs was estimated to be approximately 1.52 and 1.33 nm. This result agrees with the diameter observed by TEM.

Purified SWCNTs and unpurified raw soot were solidified by using the SPS technique [14] in a graphite die with a diameter of 10 mm at a temperature of 1000 °C under a pressure of 120 MPa. After applying the given pressure, the samples were heated to the desired temperature and held at this temperature for 5 min. The prepared specimens were disk-shaped about 10 mm in diameter and 1.5 mm in thickness, and were then polished with emery paper (#4000) into 10 mm diameter and 1.2 mm thickness. The mechanical properties such as Young's modulus and work of fracture were measured by the SP testing method [15] using miniaturized disk specimens. The SP tests were performed on a

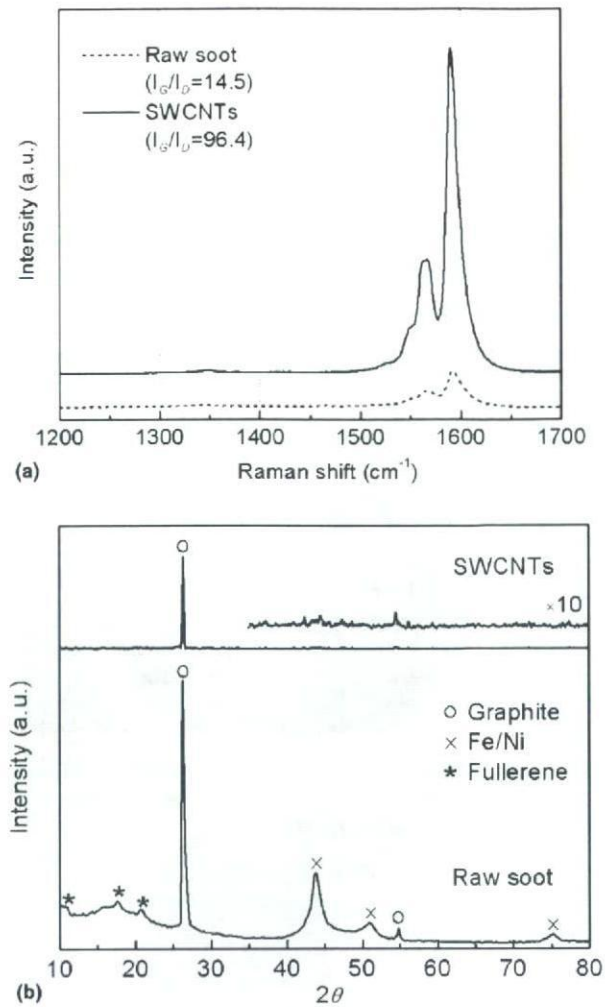

Fig. 1. (a) Raman spectra and (b) X-ray diffraction patterns of the unpurified raw soot and purified SWCNTs, respectively. The Raman intensity ratios I_G/I_D estimated from the peak position of the D-band and G-band are also indicated (a).

universal testing machine in atmospheric conditions at room temperature. The disk specimens were placed on a die having a central borehole and simply supported on the circular edge (see Ref. [15]). The load was applied at the specimen center through a puncher at a crosshead speed of 0.05 mm/min. The displacement of the specimens was monitored at the mid-point using a linear variable differential transducer (LVDT) fixed on to the testing machine.

Deformation and stress analysis for SP tests have been performed using a finite element method (FEM), assuming liner elastic response of the material [15]. In this study, the numerical data were used to compute Young's modulus and to construct a stress–normalized displacement diagram. The Young modulus of SP specimen E_{SP} was calculated from the measured initial linear slope of the load–displacement curve, which was expressed by the following equation:

$$E_{SP} = f(t/a)\frac{3a^2P(1-\nu)(3+\nu)}{4\delta\pi t^3} = f(t/a)\frac{P}{\delta}C_0, \quad (1)$$

where P is the load, δ the displacement measured at the specimen center, $f(t/a)$ the correction factor for the specimen thickness, a the borehole diameter of the supporting die (=2.1 mm), ν the Poisson's ratio, and t the specimen thickness. The maximum tensile stress along the load application point σ_{SP} can be expressed by the equation given below.

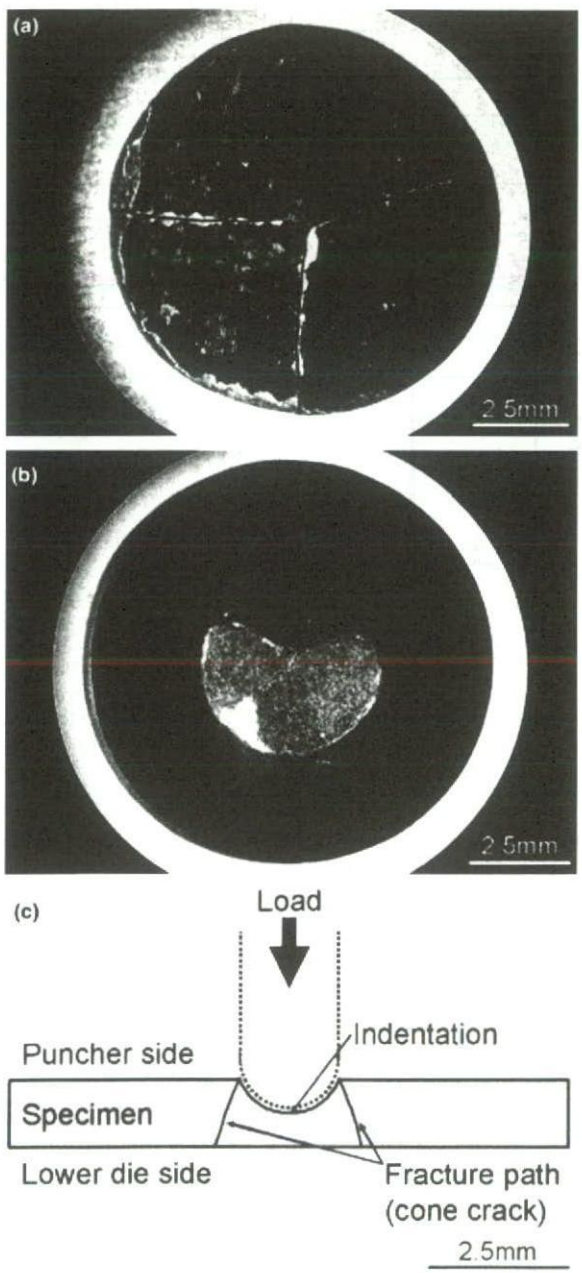

Fig. 2. Crack propagation of (a) the raw soot disk and (b) the SWCNT disk. (c) Schematic illustration of the fracture path is also shown.

$$\sigma_{SP} = \frac{P}{t^2}(1+\nu)\left[0.485\ln\frac{a}{t} + 0.52 + \frac{3}{2\pi(1+\nu)}\right] = \frac{S_0}{t^2}P. \quad (2)$$

Eqs. (1) and (2) suggest that plotting the stress versus normalized displacement curve ($\sigma_{SP} - [S_0/f(t/a)C_0t]\delta$) provides an initial slope of Young's modulus E_{SP}. The work of fracture was calculated using the area of the stress–normalized displacement curve up to the maximum load. The disk specimens made of purified SWCNTs and unpurified raw soot are referred to as SWCNT disk and raw soot disk, respectively. For each processing condition, three specimens were tested and the averaged results will be presented below.

Figs. 2 and 3 show, respectively, the fractured specimens and typical stress–normalized displacement curves for both specimens. In the case of the raw soot disks, the main crack was formed at the center of the specimen that was subjected to the maximum biaxial stress and propagated to the outer region as shown in Fig. 2(a). The specimen was broken into four pieces, which demonstrated the brittle nature of the fracture. This observation corresponds to the deformation response as shown in Fig. 3. In contrast, the purified SWCNTs produced quasi-ductile solid structures. A fractured specimen is shown in Fig. 2(b), which is also illustrated schematically in Fig. 2(c). As shown in Fig. 2(c), an indentation was formed on the specimen by the spherical puncher used for load application, and the main fracture initiated and propagated from a cone-shaped region at the edge of the indentation. A significant non-linear deformation response was observed for the SWCNT disks, as shown in Fig. 3.

The physical and mechanical properties for both specimens are shown in Table 1. The bulk density of

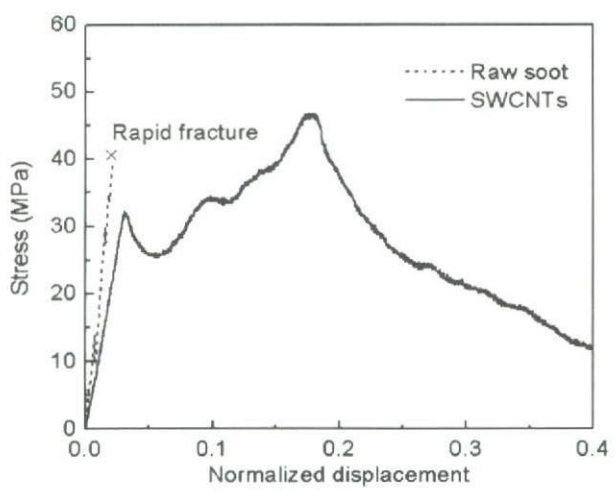

Fig. 3. Typical stress versus normalized displacement curves obtained from small punch tests. Dotted line and dark line show the fracture behavior of the raw soot disk and SWCNT disk, respectively.

Table 1
Physical and mechanical properties of the raw soot disks and SWCNT disks prepared by spark plasma sintering

Materials	Bulk density ρ (Mg/m^3)	Young's modulus E_{SP} (GPa)	Work of fracture J_{SP} (N mm)
Raw soot	1.90	0.74	1.4
SWCNTs	1.55	0.66	17.3

the raw soot disks was found to be larger than that of the SWCNT disks. This may be due to the presence of by-products such as metal particles, fullerenes and carbon materials in the raw soot disks. However, there was almost no difference in Young's modulus between the specimens. On the other hand, the work of fracture of the SWCNT disks was 12 times larger than that of the raw soot disks. The reason for the significant difference in the work of fracture may be due to the quasi-ductile fracture behavior of the SWCNT disks.

To obtain an in-depth understanding of the differences in the fracture mechanisms, the microstructural observation was carried out using a transmission electron microscope (TEM). Fig. 4 shows the typical low magnification TEM photographs of the fracture surfaces of (a) the raw soot disk and (b) the SWCNT disk. The raw soot disk consists of SWCNTs bundles (arrow A), amorphous carbon (arrow B) and metal particles (arrow C), as shown in Fig. 4(a). From the morphology of the fracture surface, it looks as if the SWCNT bundles have been pulled out from the body during the deformation and fracture of the specimen. Then, most pulled out bundles are curved and looped. However, it can be seen that the main material of fracture surface was entirely different from the structure of SWCNT bundles and the pullout was limited. In contrast, in the case of the SWCNT disk, extensive pullout of SWCNT bundles of approximately 1 μm in length were observed, and the diameter of SWCNT bundles was observed to decrease toward their tips. Fig. 4(c) is a high-resolution TEM photograph of the fracture surface of SWCNT disk. From the TEM photograph, it can be seen that numerous bundles containing 10–30 nanotubes protrude from the fracture surface, and the average diameter of SWCNTs in the bundles was 1.58 and 1.39 nm, which is in approximate agreement with the diameter of SWCNTs before the solidification process. Detailed observation of the fracture surface indicates that no breakage of SWCNTs occurred in the bundles for both cases. These experimental results indicate that the brittleness of the raw soot disks may be due to the inherent brittleness of carbon materials such as amorphous carbon and graphite, which possess no effective stress transfer capability between the bundles and

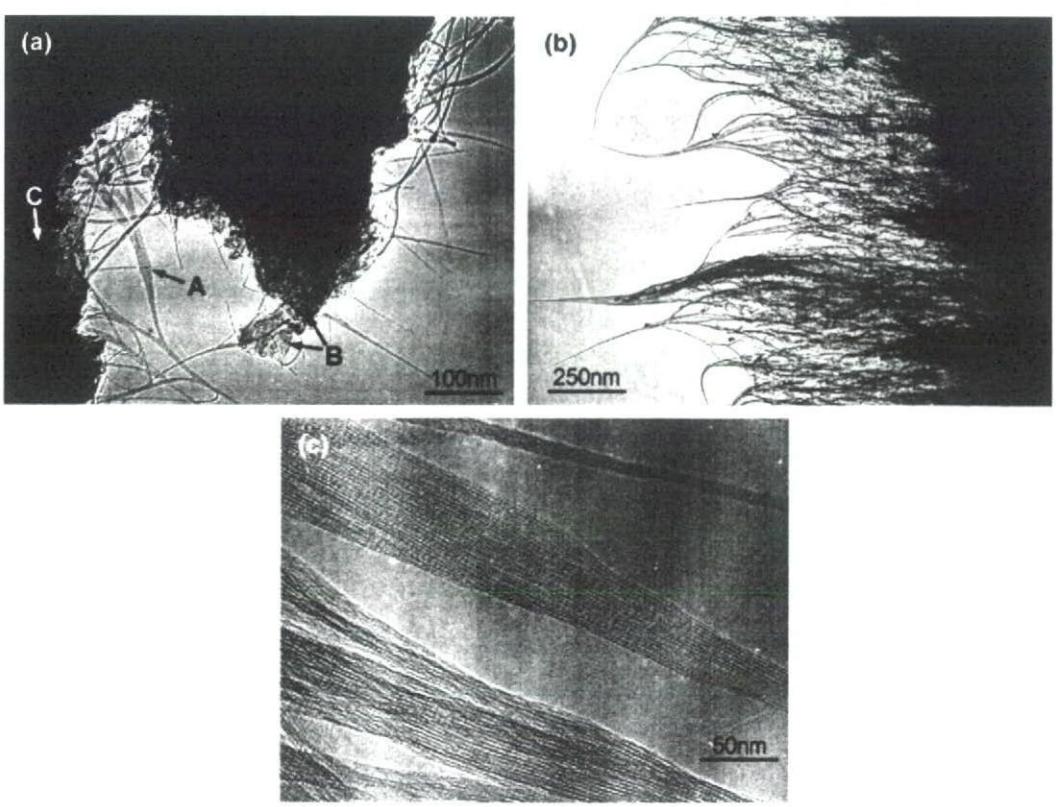

Fig. 4. Typical low magnification TEM photographs of fracture surfaces of (a) the raw soot disk and (b) the SWCNT disk. (c) A high-resolution TEM photograph of fracture surfaces of SWCNT disk.

carbon materials. In contrast, the failure in the SWCNT disks occurred via intra-bundle sliding between SWCNTs, within and between the bundles. The significant non-linear deformation response of the SWCNT disks may be due to the pullout behavior associated with the slippage of SWCNTs held by weak van der Waals interactions.

In this study, we have successfully produced SWCNT disks without any additives, employing the SPS method. This solidification method enables us to produce quasi-ductile solid structures composed of purified SWCNTs with Young's modulus of 0.66 GPa. In contrast, unpurified raw soot produced brittle solids structures with Young's modulus of 0.74 GPa. However, Young's modulus of the purified SWCNT disks is still lower than the individual SWCNTs due to the sliding of SWCNTs within the bundles. Work is in progress to improve the mechanical properties of the binder-free purified SWCNT disks by introducing effective chemical bonding between SWCNTs, within and between the bundles.

Acknowledgments

This work was supported by the Japan Ministry of Health, Labor and Welfare under Grants-in-Aid for Research on Advanced Medical Technology and the 21st Century COE Program Grant of the International COE of Flow Dynamics, which were supported by Ministry of Education, Culture, Sports, Science and Technology. We thank the staff at the Laboratory for Advanced Material of the Tohoku University for their assistance.

References

[1] Yu MF, Files BS, Arepalli S, Ruoff RS. Phys Rev Lett 2000;84:5552.
[2] Li F, Cheng HM, Bai S, Su G. Appl Phys Lett 2000;77:3161.
[3] Ajayan PM, Schadler LS, Giannaris C, Rubio A. Adv Mater 2000;12:750.
[4] Flahaut E, Peigney A, Laurent CH, Marliere CH, Chastel F, Rousset A. Acta Mater 2000;48:3803.
[5] Ma RZ, Wu J, Wei BQ, Liang J, Wu DH. J Mater Sci 1998;33:5243.
[6] Zhan GD, Kuntz JD, Wan JW, Mukherjee AK. Nature Mater 2003;2:38.
[7] Seraphin S, Zhou D. Appl Phys Lett 1994;64:2087.
[8] Thess A, Lee R, Nikolaev P, Dai H, Petit P, Robert J, et al. Science 1996;273:483.
[9] Dai H, Rinzler AG, Nikolaev P, Thess A, Colbert DT, Smalley RE. Chem Phys Lett 1996;260:471.
[10] Tohji K, Takahashi H, Shimizu N, Jeyadevan B, Matsuoka I, Saito Y, et al. J Phys Chem 1997;101:1974.
[11] Kataura H, Kumazawa Y, Maniwa Y, Ohtsuka Y, Sen R, Suzuki S, et al. Carbon 2000;38:1691.
[12] Sato Y, Jeyadevan B, Hatakeyama R, Kasuya A, Tohji K. Chem Phys Lett 2004;385:323.
[13] Bachilo SM, Strano MS, Kittrell C, Hauge RH, Smalley RE, Weisman RB. Science 2002;298:2361.
[14] Omori M. Mater Sci Eng A 2000;287:183.
[15] Okuda S, Saito M, Hashida T, Takahashi H. Trans JSME A 1991;57:940.

Available online at www.sciencedirect.com
SCIENCE DIRECT
Chemical Physics Letters 417 (2006) 288–292
CHEMICAL PHYSICS LETTERS
www.elsevier.com/locate/cplett

Electrically triggered insertion of single-stranded DNA into single-walled carbon nanotubes

Takeru Okada [a,*], Toshiro Kaneko [a], Rikizo Hatakeyama [a], Kazuyuki Tohji [b]

[a] *Department of Electronic Engineering, Tohoku University, 6-6-05 Aramaki-Aza, Aoba-ku, Sendai, Miyagi 980-8579, Japan*
[b] *Graduate School of Environmental Studies, Tohoku University, Sendai 980-8579, Japan*

Received 8 June 2005; in final form 3 October 2005
Available online 2 November 2005

Abstract

The formation of DNA encapsulated carbon nanotubes, which are expected to modify electronic properties of carbon nanotubes, is for the first time demonstrated using a modified electrophoresis method. Radio-frequency and direct-current electric fields are applied to the DNA solution in order to stretch random-coil-shaped DNA and irradiate DNA to carbon nanotubes that are coated onto electrodes immersed in the DNA solution, respectively. Transmission electron microscopy and Raman scattering spectroscopy analyses reveal that DNA can be encapsulated into the carbon nanotubes. In this procedure, the key for the formation of DNA encapsulated carbon nanotubes is found to irradiate the stretched-shaped DNA to the carbon nanotubes.

1. Introduction

Much attention and a variety of studies have been devoted to electronic, chemical, and physical modifications of single-walled carbon nanotubes (SWNTs). The modification modes of SWNTs are roughly divided into two approaches. One is intercalation of materials between bundles [1–3] or attachment to outside walls of SWNTs [4–6]. The other is encapsulation of materials in the inside of SWNTs [7–12]. Intercalation can modify electronic properties of SWNTs, which does not require so complicated procedure in general. However, intercalation is inevitably beset with problems for future applications, for example, air-stability of the intercalated SWNTs is one of the most fatal issues for the realization of novel electronic devices because the intercalated functional materials are exposed to the air. On the contrary, functional-material encapsulated SWNTs are expected to ensure this air stability, because the functional materials are inserted inside the hollow regions of SWNTs and are isolated from the air. Although the alkali metal [13], C_{60} [14], and organic molecules [12] have been used as the encapsulated functional materials so far, DNA is also an interesting material for the future applications not only in biology but also other fields because of their unique properties. DNA consists of four kinds of bases, each of which has a different electronic property [15], and the base sequence has come to be easily controlled in recent years.

To the best of our knowledge, there have been some papers which relate to the combination between SWNTs and DNA [16,17]. However, the approaches of the papers are limited to the utilization of outside wall of SWNTs. On the contrary, our viewpoint is focused upon the utilization of inside nano-space of SWNTs innovating DNA. Thus, DNA is expected to reflect its electronic properties in characterizing SWNTs when DNA is encapsulated into SWNTs. As a result, encapsulated DNA is predicted to modify electronic properties of the SWNTs in accordance with changing length and base sequence of DNA. Here, we demonstrate for the first time the formation of DNA encapsulated SWNTs (DNA@SWNTs) that are expected to yield great potential for nano-scale electronics.

* Corresponding author. Fax: +81 22 263 9225.
E-mail address: okada@ecei.tohoku.ac.jp (T. Okada).

0009-2614/$ - see front matter © 2005 Elsevier B.V. All rights reserved.
doi:10.1016/j.cplett.2005.10.030

2. Experimental

In this study, SWNTs are purified in advance, which were produced by an arc discharge method [18]. After purification, SWNTs are treated by heat for the opening of SWNTs tips. The heat treatment is performed in the air for 30 min at 750 K. The formation of open-ended SWNTs is confirmed by the formation of C_{60} encapsulated SWNTs in the same way as reported by Bandow et al. [9]. The purity of SWNTs remains high even after heat treatment for the opening of the tip. The peak intensity ratio of G band to D band (G/D ratio) in Raman spectra of SWNTs after heat treatment is more than 50 when excitation energy of laser is 2.54 eV. The average diameter of SWNTs is about 1.5 nm and the diameter is distributed in the rage of 1.2–1.7 nm. We adopt two kinds of single-stranded DNA (ssDNA) with different lengths as a material for the insertion into SWNTs. One ssDNA consists of 15 adenines (15A-DNA) and the other consists of 30 adenines (30A-DNA). Since the length of 10 bases is estimated to be 3.4 nm on the assumption that DNA molecules make up a helix conformation, the lengths of 15A-DNA and 30A-DNA are about 5 and 10 nm, respectively.

Fig. 1 shows schematic of an experimental apparatus to irradiate ssDNA which is dissolved into water to open-ended SWNTs. Open-ended SWNTs are coated onto aluminum electrodes (anode and cathode) which are submerged in the ssDNA solution. The distance of the two electrodes is 1 mm and the volume of the ssDNA solution is 5 ml. When a direct current (DC) bias voltage (V_{DC}) is applied to the anode electrode, ssDNA is considered to be irradiated to it in the same way as an electrophoresis

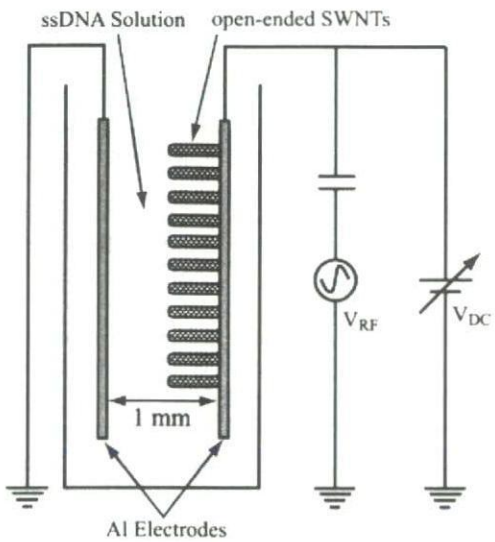

Fig. 1. Schematic of an experimental apparatus for the formation of DNA encapsulated carbon nanotubes, where both the DC and RF electric fields can independently be applied to the ssDNA solution. Open-ended SWNTs are considered to be oriented perpendicularly to the anode electrode along the electric field, which is formed by applying the DC and/or RF voltages to the electrodes.

method because DNA molecules constitute the phosphoric acid group which has a negative charge. Since DNA molecules make up the random-coiled conformation in solution, however, it is difficult to encapsulate DNA molecules directly into SWNTs. When an radio frequency (RF) electric field is externally applied to DNA, on the other hand, dominant dipole moment is induced along DNA axis because of their high anisotropicity, resulting in stretching DNA molecules parallel to the external electric field due to the interaction between the external field and the induced dipole. In addition, this kind of ponderomotive force [19] generated by the RF electric field is supposed to work on moving the stretched and orientated DNA molecules to both the anode and the cathode. Thus, we superimpose the radio frequency voltage (V_{RF}) upon V_{DC} in order to stretch DNA molecules and irradiate them to the electrodes, as given in Fig. 1 [20,21]. Furthermore, in the case that the DC and/or RF electric fields are applied, SWNTs are considered to stand on the electrodes along the electric fields and the orientation of the SWNTs is expected to be perpendicular to the electrodes [14,19].

3. Results and discussion

After the irradiation of the DNA molecules to the electrodes, they are adsorbed onto the aluminum surface of the electrodes and the adsorption is maintained semipermanently [15]. Furthermore, the aggregation of ssDNA is initiated at the aluminum surface by the existence of the aluminum ions coming from the V_{DC} and/or V_{RF} applied electrodes. Therefore, the amount of the irradiated DNA molecules to the anode–electrode surface can be estimated by measuring the concentration of the DNA solution after applying V_{DC} and/or V_{RF}. Here, UV–vis absorption spectra of the DNA solution are available for calculating the DNA concentration.

Fig. 2a presents a typical UV–vis absorption spectrum of the ssDNA solution, where we can find a specific absorption peak around 260 nm originating from the DNA molecules. Then, the concentration of the solution is obtained using the peak intensity dependence under the normalization that the value of 1 in absorbance corresponds to about 35 μg/ml. The time evolution of the calculated concentration of the DNA solution with V_{DC} as a parameter is plotted in Fig. 2b, where the concentration decreases with the irradiation time and an increase in V_{DC}. The results indicate that the DNA irradiation is controlled by changing the DC bias voltage and irradiation time. In the case of $V_{DC} = 10$ V, almost all of the DNA molecules appear to be irradiated to the anode. Based on the DNA-concentration results, the irradiation of DNA to the open-ended SWNTs to form the DNA encapsulated SWNTs is performed within 10 min for $V_{DC} = 10$ V in the following measurements.

Fig. 3 shows spectra of Raman scattering spectroscopy in the range of the radial breathing mode of SWNTs, which are measured by using different laser excitation energies (a)

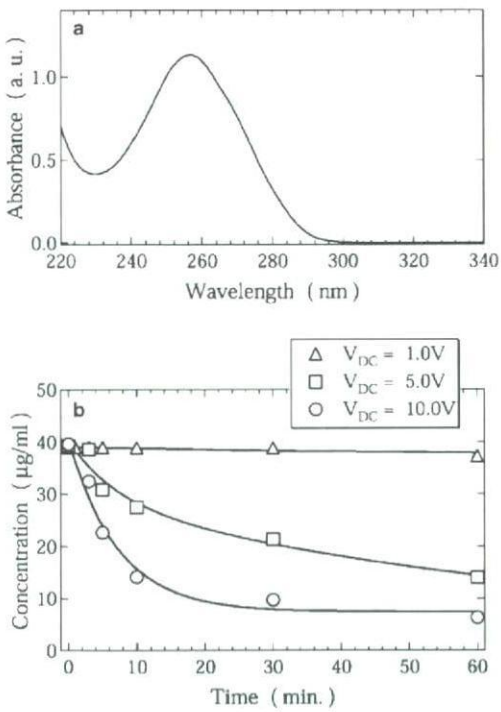

Fig. 2. (a) Typical UV–vis absorption spectrum of ssDNA solution. (b) Time evolution of the concentration of ssDNA solution with V_{DC} as a parameter.

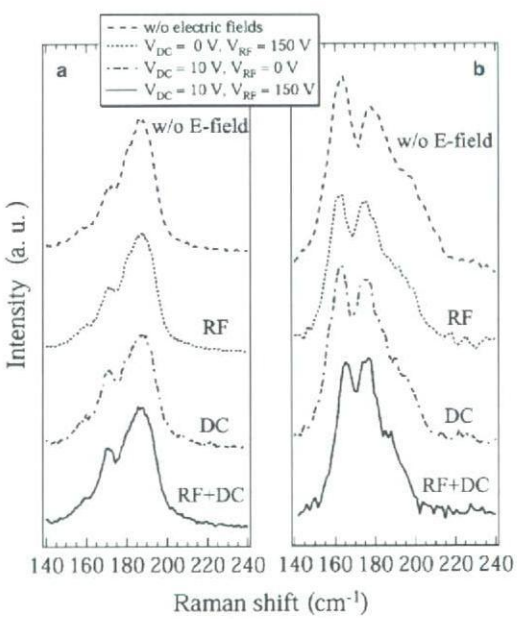

Fig. 3. Raman spectra of SWNTs after ssDNA (15A-DNA) irradiation. Excitation energies of laser are (a) 2.41 eV and (b) 2.54 eV, respectively.

2.41 eV and (b) 2.54 eV. The Raman spectra of SWNTs after the ssDNA irradiation are obtained under the dried condition after the removal of DNA attached on the surface of SWNTs by washing with water. The shape of the spectra and the peak intensity are found to be different between the cases with and without applying electric fields, especially in the case of the excitation energy of 2.54 eV. The changes of the peak intensity in the range of the radial breathing mode (RBM) are considered to be one of the phenomena associated with charge transfer between ssDNA and carbon nanotubes. Although the effect of charge transfer may be very small, the signal of RBM is considered to be very sensitive to the condition of the SWNT inner region. As a result, even a slight effect of the charge transfer has the possibility of changing RBM, giving indirect evidence of the encapsulation of other materials inside SWNTs.

When only the DC electric field is applied (DC), the spectra shapes become sharp (Fig. 3a, b) and the intensity ratio of two peaks observed in Fig. 3b is changed compared with the case where no electric field is applied (w/o E-field). Since the DC electric field is predicted to induce the driving force enhancing the insertion of the DNA molecules as described above, such features in the Raman spectra are due to the effect of the DNA irradiation triggered by the DC field application. According to observations by high-resolution transmission electron microscopy (HR-TEM), however, the yield of DNA@SWNTs seems to be not so high under this condition.

On the other hand, an appreciable difference is recognized between the cases with and without RF electric field applied SWNTs (RF). In this situation, a part of 15A-DNA can be stretched by the RF electric field and inserted into SWNTs even in the absence of strong external driven force such as a DC electric field, because the length of 15A-DNA is about 5 nm and its diameter is comparatively similar to the diameter of SWNTs (1.2–1.7 nm). It is plausible that ssDNA can be inserted to some extent into opened-SWNTs without the positive DNA irradiation, which is not inconsistent with a simulation study reported by Gao et al. [22]. Based on the Raman analyses, however, the yield is estimated to be quite low when only the RF electric field is applied in the absence of the DC electric field.

Furthermore, in the case that both V_{DC} and V_{RF} are applied simultaneously, in other words, stretched ssDNA is irradiated (RF + DC), the spectrum shape becomes sharper, for example, a hump around 185 cm^{-1} in Fig. 3b disappears. In addition, we can perceive some changes in the peak intensities around 180 cm^{-1} in Fig. 3a and at 164 and 178 cm^{-1} in Fig. 3b. These results imply that the encapsulation yield of ssDNA into open-ended SWNTs is considerably enhanced when both the DC and RF electric fields are superimposed.

Based on the results in Fig. 3, the rate of encapsulation of ssDNA into SWNTs is considered to be estimated with a decrease in the peak intensity at 164 cm^{-1} compared with the peak intensity at 178 cm^{-1}. The ratio of peak intensity at 164 cm^{-1} to that at 178 cm^{-1} in the Raman spectrum is plotted as a function of V_{DC} for $V_{RF} = 50$ V in Fig. 4, where laser excitation energy is 2.54 eV. The ratio decreases with an increase in the applied DC electric field. As already shown in Fig. 2, the amount of irradiation of DNA nega-

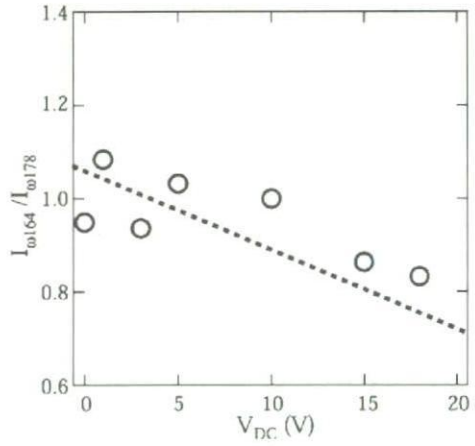

Fig. 4. The peak intensity ratio of 164–178 cm^{-1} in Raman spectra of SWNTs after ssDNA irradiation as a function of V_{DC} for $V_{RF} = 50$ V. Laser excitation energy is 2.54 eV.

tive ions is found to depend on the applied DC electric field. Thus, when the conformation of DNA is stretched by the RF electric field, the encapsulation ratio resultantly depends on the DNA ion irradiation. Therefore, the large amount of stretch-shaped ssDNA irradiation leads to the improvement of the yield of DNA@SWNTs.

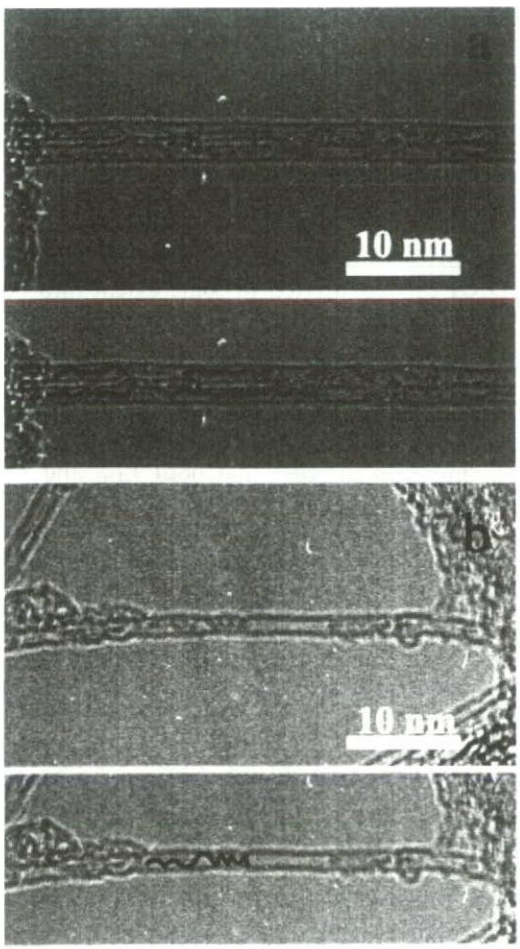

Fig. 5. HR-TEM images of SWNTs after ssDNA irradiation in the cases of using (a) 15A-DNA (about 5 nm lengths) and (b) 30A-DNA (about 10 nm lengths). The black lines in images indicate encapsulated materials.

The intensive observation of SWNTs undergoing the DNA irradiation is performed using HR-TEM, where the acceleration voltage is 200 kV. Fig. 5a presents HR-TEM images of SWNTs after the DNA irradiation under the condition of $V_{DC} = 10$ V and $V_{RF} = 20$ V in the case of 15A-DNA. The one-dimensional materials appear to be encapsulated in SWNTs, where the black lines in the images indicate the encapsulated materials. The length of the encapsulated material is about 5 nm which corresponds to that of 15A-DNA. In the case of using 30A-DNA, the HR-TEM image is shown in Fig. 5b, where the DNA irradiation condition is $V_{DC} = 10$ V and $V_{RF} = 150$ V. The encapsulated material is also observed and its length is estimated to be about 10 nm. Besides, 30A-DNA is found to form a helical conformation inside SWNTs and seems to be adsorbed onto the inner wall. Based on the TEM observation, it is likely that the bases, hydrophobic part of DNA, and the certain length of ssDNA tend to be adsorbed onto the inner wall and to form the helical conformation in SWNTs, respectively [23].

Since the ssDNA irradiation method described here utilizes negatively charged part of ssDNA molecules, i.e., phosphoric acid group in the ssDNA molecules and the stretch of ssDNA molecules is caused by the interaction of the permittivity of ssDNA with applied external electric fields, the effect of irradiation and stretch is independent of the base sequence. Therefore, this formation method of DNA encapsulated SWNTs can be applied to not only specific base sequence of DNA consisting of, for example, only adenines, but also any base sequence.

4. Summary

In conclusion, the ssDNA encapsulated SWNTs are created for the first time by applying DC and RF electric fields to the DNA solution. Based on the Raman spectrum and HR-TEM analyses, the encapsulation of ssDNA into open-ended SWNTs is enhanced when both the DC and RF electric fields are simultaneously superimposed. It is found that ssDNA is adsorbed onto the inner wall of SWNTs and exists in the form of helical conformation when the length of ssDNA is enough decisive. These results lead to a claim that a process of superimposing RF electric field upon DC electric field plays a decisive role in the DNA encapsulated SWNT formation in this solution-phase procedure. The ssDNA encapsulated SWNTs could have a possibility of novel electrical modification of SWNTs.

Acknowledgments

The authors thank Dr. Y. Sato and Mr. K. Motomiya for their technical support. This research was partly carried out at the Laboratory for Nanoelectronics and Spintronics,

Research Institute of Electrical Communication, Tohoku University. Part of this work was carried out under the Cooperative Research Project Program of the Research Institute of Electrical Communication, Tohoku University. This work was also supported by a Grant-in-Aid for Scientific Research from the Ministry of Education, Culture, Sports, Science and Technology, Japan, and Tohoku University 21st COE (Center of Excellence) Program.

References

[1] R.S. Lee, H.J. Kim, J.E. Fischer, A. Thess, R.E. Smalley, Nature 388 (1997) 255.
[2] A.M. Rao, P.C. Eklund, S. Bandow, A. Thess, R.E. Smalley, Nature 388 (1997) 257.
[3] J. Kong, C. Zhou, E. Yenilmez, H. Dai, Appl. Phys. Lett. 77 (2000) 3977.
[4] S.E. Baker, W. Cai, T.L. Lasseter, K.P. Weidkamp, R.J. Hamers, Nano Lett. 2 (2002) 1413.
[5] K.A. Williams, P.T.M. Veenhuizen, B.G. de la Torre, R. Eritja, C. Dekker, Nature 420 (2002) 761.
[6] H. Cai, X. Cao, Y. Jiang, P. He, Y. Fang, Anal. Bioanal. Chem. 375 (2003) 287.
[7] R. Hatakeyama, T. Hirata, G.-H. Jeong, Plasma Source Sci. Technol. 13 (2004) 108.
[8] S. Bandow, M. Takizawa, H. Kato, T. Okazaki, H. Shinohara, S. Iijima, Chem. Phys. Lett. 347 (2001) 23.
[9] S. Bandow, M. Takizawa, H. Hirahara, M. Yudasaka, S. Iijima, Chem. Phys. Lett. 337 (2001) 48.
[10] H. Kataura, Y. Maniwa, T. Kodama, K. Kikuchi, K. Hirahara, K. Suenaga, S. Iijima, S. Suzuki, Y. Achiba, W. Kratschmer, Synth. Met. 121 (2001) 1195.
[11] R. Pfeiffer, H. Kuzmany, W. Plank, T. Pichler, H. Kataura, Y. Achiba, Diam. Relat. Mater. 11 (2002) 957.
[12] T. Takenobu, T. Takano, M. Shiraishi, Y. Murakami, M. Ata, H. Kataura, Y. Achiba, Y. Iwasa, Nature Mater. 2 (2003) 683.
[13] G.-H. Jeong, A.A. Frajian, R. Hatakeyama, T. Hirata, T. Yaguchi, K. Tohji, H. Mizuseki, Y. Kawazoe, Phys. Rev. B 68 (2003) 075410.
[14] G.-H. Jeong, T. Hirata, R. Hatakeyama, K. Tohji, K. Motomiya, Carbon 40 (2002) 2247.
[15] K.-H. Yoo, D.H. Ha, J.-O. Lee, J.W. Park, J. Kim, J.J. Kim, H.-Y. Lee, T. Kawai, H.-Y. Choi, Phys. Rev. Lett. 87 (2001) 198102.
[16] N. Nakashima, S. Okuzono, H. Murakami, T. Nakai, K. Yoshikawa, Chem. Lett. 32 (2003) 456.
[17] M. Zheng, A. Jagota, E.D. Semke, B.A. Diner, R.S. Mclean, S.R. Lusting, R.E. Richardson, N.G. Tassi, Nature Mater. 2 (2003) 338.
[18] K. Tohji, T. Goto, H. Takahashi, Y. Shinoda, N. Shimizu, B. Jeyadevan, I. Matsuoka, Y. Saito, A. Kasuya, T. Ohsuna, K. Hiraga, Y. Nishina, Nature 383 (1996) 679.
[19] R. Krupke, F. Hennrich, H.B. Weber, M.M. Kappes, H.V. Lohneysen, Nano Lett. 3 (2003) 1019.
[20] M. Washizu, O. Kurosawa, IEEE Trans. Ind. Appl. 26 (1990) 1165.
[21] S. Suzuki, T. Yamanashi, S. Tazawa, O. Kurosawa, M. Washizu, IEEE Trans. Ind. Appl. 34 (1998) 75.
[22] H. Gao, Y. Kong, D. Cui, C.S. Ozakan, Nano Lett. 3 (2003) 471.
[23] M. Zheng, A. Jagota, M.S. Strano, A.P. Santos, P. Barone, S.G. Chou, B.A. Diner, M.S. Dressselhaus, R.S. Mclean, G.B. Onoa, G.G. Samsonidze, E.D. Semke, M. Usrey, D.J. Walls, Science 302 (2003) 1545.

Journal of Solid Mechanics and Materials Engineering

Vol. 1, No. 7, 2007

Mechanical Properties of Single-Walled Carbon Nanotube Solids Prepared by Spark Plasma Sintering*

Go YAMAMOTO**, ***, Yoshinori SATO***, Toru TAKAHASHI****, Mamoru OMORI****, Kazuyuki TOHJI*** and Toshiyuki HASHIDA****

**Institute of Fluid Science, Tohoku University,
2-2-1 Kataura, Aoba-ku, Sendai 980-8577, Japan
E-mail: gyamamoto@rift.mech.tohoku.ac.jp
***Graduate School of Environmental Studies, Tohoku University,
6-6-11-1305, Aza-Aoba, Aramaki, Aobaku, Sendai 980-8579, Japan
****Fracture and Reliability Research Institute, Tohoku University,
6-6-11-707, Aza-Aoba, Aramaki, Aobaku, Sendai 980-8579, Japan

Abstract

In this paper, a spark plasma sintering (SPS) method was employed to solidify single-walled carbon nanotubes (SWCNTs) only, and the effect of processing conditions on the mechanical properties of the SWCNT solids were examined using a small punch (SP) testing method. The sintering temperatures used was in the range of 600~1400°C, and the sintering pressures used was 40 MPa and 120 MPa. It was demonstrated that the SPS method allowed SWCNTs to be solidified, without any additives. The experimental results showed that the purification of raw soot was critically importance. The SWCNT solids prepared from purified raw soot showed significant non-linear deformation response, producing quasi-ductile fracture behavior. In contrast, raw soot produced brittle solids. The Young's modulus, fracture strength and work of fracture increased with the increasing sintering temperature and pressure. The Raman and SEM analyses showed that the amount of the graphite-like materials were observed to increase with the increasing temperature and pressure, which indicate that the structure of the SWCNTs was changed partially into the graphite-like materials. The formation of graphite-like materials increased tendency of brittle fracture in the SWCNT solids. TEM observations revealed that the fracture surfaces of the SWCNT solids were characterized by pull out of SWCNT bundles. This observation suggests that it may be possible to improve the mechanical properties of SWCNT solids by increasing the cohesion between SWCNTs.

Key words: Single-Walled Carbon Nanotube, Spark Plasma Sintering Method, Small Punch Testing Method, Young's Modulus, Work of Fracture

1. Introduction

Recent experimental studies have amply demonstrated that individual single-walled carbon nanotubes [1][2] (SWCNTs) have an extremely high Young's modulus and tensile strength [3]-[5]. Researchers have mostly examined the possible applications of SWCNTs in various matrices, and characterized the properties and microstructures of these composite materials [6][7]. However, the production of SWCNT-reinforced composites with unprecedented mechanical properties is yet to be realized. Additionally, in order to take full

*Received 25 Dec., 2006 (No. T-04-0645)
Japanese Original : Trans. Jpn. Soc. Mech. Eng., Vol. 71, No. 702, A (2005), pp. 330-337 (Received 3 June, 2004)
[DOI: 10.1299/jmmp.1.854]

advantage of the intrinsic mechanical and physical properties of SWCNTs, it is necessary to produce solid structures that are composed solely of the SWCNTs.

In this study, we have successfully produced binder-free SWCNT solids with purified SWCNTs by using a spark plasma sintering (SPS) method [8], and the mechanical properties of the disk specimens were investigated by a small punch (SP) testing method [9]. Here, the effects of processing temperatures and pressures on the mechanical properties of the resultant solids were investigated. Raw soot synthesized by conventional methods commonly contains metal particles and various forms of carbon. Therefore, the effect of the impurities on the mechanical properties and microstructures was also investigated by comparing the results obtained from the disk specimens made of the purified SWCNTs and raw soot containing by-products and SWCNTs.

2. Experimental

2.1 Purification Procedure for SWCNTs and Solidification Method

SWCNTs were synthesized by a direct current arc discharge between a pure graphite cathode and a metal loaded graphite anode [10]. A pure graphite rod (Wako Pure Chemical Industries, 99.9 % purity), 16 mm in diameter and 50 mm in length, and a 6 mm in diameter and 80 mm in length graphite rod loaded with Fe and Ni powders (Wako Pure Chemical Industries, 99.99 % purity) were used as cathode and anode, respectively. The mixing ratio of Fe, Ni and graphite powder for synthesis of SWCNTs was 1:1:3 by weight. The arc discharge was carried out under a helium atmosphere of 100 Torr. The discharge current was 70 A, and during the discharge, the gap between the electrodes was maintained at about 3 mm by manually advancing the consumed anode. The raw soot containing SWCNTs produced by the arc discharge method was retrieved from the upper wall and the roof of the chamber and was homogenized by mixing together regardless of the different sampling locations. In the raw soot, SWCNTs coexist with many by-products such as metal particles, fullerenes and amorphous carbon. Therefore, SWCNTs were separated step by step from the impurities using the following purification process. First, the fullerenes and the amorphous carbon were burned out by heating approximately 600 mg of raw soot at 450°C and keeping for 30 min in air. Then, the residual soot was heated up to 500°C and kept for 30 min in air to burn out the graphitic layers surrounding metal particles. Finally, the metal particles were washed out from the soot by treating with 6 M hydrochloric acid solution. The processed soot was filtered and rinsed with deionized water.

Purified SWCNTs and raw soot were solidified by using the SPS technique in a graphite die with an inner diameter of 10 mm. The processing temperatures and pressures used for preparation of disk specimens are summarized in Table 1. After applying the given pressure, the samples were heated to the desired temperature and held at this temperature for 5 min. The prepared specimens were disk-shaped about 10 mm in diameter and 1.5~1.8 mm in thickness, and were then polished with emery paper (#4000) into 10 mm in diameter and 1.2 mm in thickness. Purified SWCNTs was also consolidated by mechanical compaction only at room temperature and pressures of 40 and 120 MPa.

Table 1 Processing conditions of SWCNT solids prepared by spark plasma sintering.

Materials	Sintering temperature (°C)	Sintering pressure (MPa)	Holding time (min)
Raw soot	1000	120	5
Purified SWCNTs	600-1400	40, 120	5

2.2 Evaluation Method

The mechanical properties such as Young's modulus and work of fracture were measured by the SPS testing method using miniaturized disk specimens. Figure 1 shows schematic illustration of the experimental setup which was used in the present work to evaluate the mechanical properties of the SWCNT solids. The SP tests were performed on a universal testing machine (Instron 1185, Instron Corporation) in atmospheric conditions at room temperature. The disk specimens were placed on a die having a central borehole and simply supported on the circular edge. The load was applied at the specimen center through a puncher at a crosshead speed of 0.05 mm/min. The displacement of the specimens was monitored at the mid-point using a linear variable differential transducer (LVDT; DTH-A-50, Kyowa Electronic Instruments) fixed on to the testing machine.

Deformation and stress analysis for SP tests have been performed using an element method (FEM), assuming liner elastic response of the material [9]. In this study, the numerical data were used to compute Young's modulus and to construct stress-normalized displacement diagram. The Young's modulus of SP specimen E_{SP} was calculated from the measured initial linear slope of the load-displacement curve, which was expressed by the following equation:

$$E_{SP} = f(t/a)\frac{3a^2P(1-\nu)(3+\nu)}{4\delta\pi t^3} = f(t/a)\frac{P}{\delta}C_0, \tag{1}$$

where P is the load, δ the displacement measured at the specimen center, $f(t/a)$ the correction factor for the specimen thickness, a the borehole diameter of the supporting die (=2.1 mm), ν the Poisson's ratio, and t the specimen thickness (=1.2 mm). The maximum tensile stress along the load application point σ_{SP} can be expressed by the equation given below.

$$\sigma_{SP} = \frac{P}{t^2}(1+\nu)\left[0.485\ln\frac{a}{t} + 0.52 + \frac{3}{2\pi(1+\nu)}\right] = \frac{S_0}{t^2}P. \tag{2}$$

Equations (1) and (2) suggest that plotting the stress versus normalized displacement curve (σ_{SP}-$[S_0/f(t/a)C_0t]\delta$) provides an initial slope of Young's modulus E_{SP}. The work of fracture was calculated using the area of the stress-normalized displacement curve up to the maximum load. The disk specimens made of purified SWCNTs and raw soot are referred to

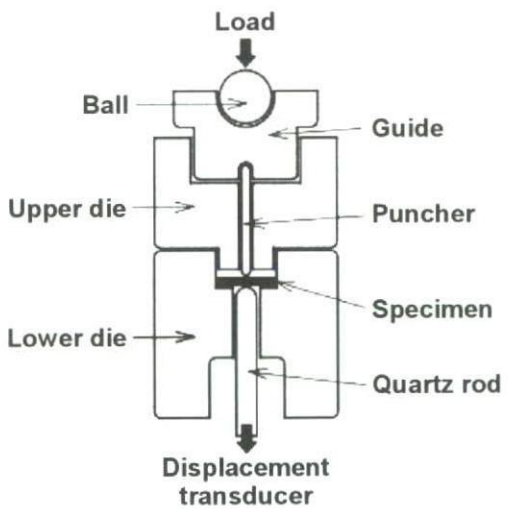

Fig. 1 Schematic illustration of small punch testing method.

as SWCNT solid and raw soot solid, respectively. For each processing condition, two specimens were tested and the averaged results will be presented below.

The structural analysis of the purified SWCNTs and raw soot was carried out using a Raman spectroscopy (T64000, HORIBA) with Ar ion laser, powder X-ray diffractometer (M21, Mac Science) with Cu Kα X-ray source and scanning electron microscopy (SEM; S-4700, Hitachi). The fracture surface was investigated by using a transmission electron microscopy (TEM; HF-2000, Hitachi).

3. Results and Discussion

3.1 Evaluation of the Purification Procedure and Characterization of Purified SWCNTs

In this study, macroscopic SWCNT solid was successfully solidified by SPS. Figures 2 and 3 show the Raman spectrum of the raw soot and purified SWCNTs, respectively. Abundance of SWCNTs in the each sample estimated from the Raman-scattering intensity ratio I_G/I_D is also indicated. Raman-scattering peaks corresponding to E_{2g} vibration mode near 1570 and 1590 cm^{-1} are due to the zone-folding effect of the SWCNTs [11]. Since the peak at 1350 cm^{-1} corresponds to a Raman-active mode of defective carbon network, the intensity roughly proportional to the amount of amorphous carbon in the sample. Hence, the relative Raman-scattering intensity ratio I_G/I_D of the peaks at 1350 cm^{-1} (D-band) and 1590 cm^{-1} (G-band) is a convenient index for the evaluation of SWCNT abundance ratio in the sample. It can be seen from Figs. 2 and 3 that the G-band peak intensity of the purified SWCNTs increased from 14.5 to 96.4 compared with that of the raw soot. Furthermore, the I_G/I_D of the purified SWCNTs was about seven times larger than that of raw soot, without any change in each peak position. Figures 4 and 5 show the typical SEM images of the raw

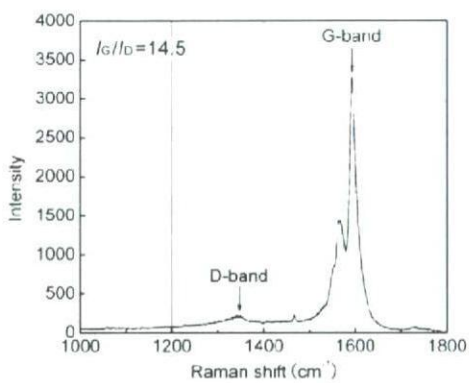

Fig. 2 Raman spectrum of the raw soot.

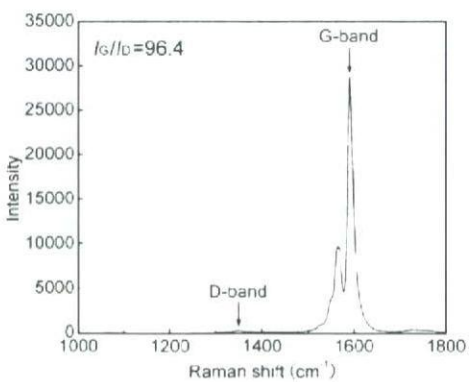

Fig. 3 Raman spectrum of the purified SWCNTs.

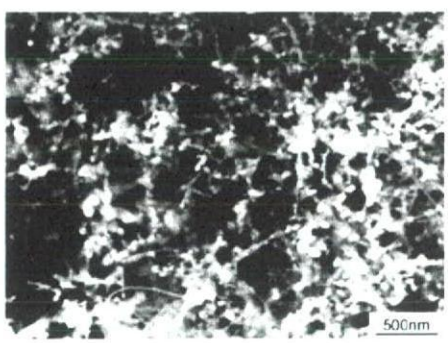

Fig. 4 SEM image of the raw soot.

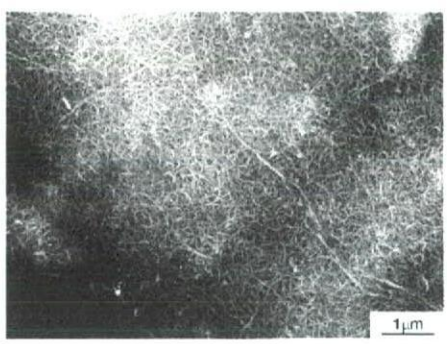

Fig. 5 SEM image of the purified SWCNTs.

soot and purified SWCNTs, respectively. The SEM image of the raw soot shows the SWCNT bundles coexisted with many by-products such as amorphous carbon. According to the XRD analysis of the raw soot [12], data shows the presence of C_{60}, graphite and metals. In contrast, the purified SWCNT were free of C_{60} and metals, showing only graphite peak. However, a trace amount of carbon materials with about 0.5 mm in diameter other than SWCNTs was observed as shown in Fig. 5. The length and diameter of the purified SWCNT bundle, estimated using SEM, were about 3~22 μm and 87 nm, respectively. These results suggest that highly pure SWCNTs have been obtained under the above-mentioned conditions, even though only a trace amount of carbon materials are present in the purified SWCNTs. The high purity of the SWCNT prepared has also been supported by thermogravimetric analysis.

3.2 Evaluation of Mechanical Properties

3.2.1 Effect of Impurities

In this work, we have successfully produced SWCNT solids with out any additives by using SPS method. Here, in order to reveal the effect of impurities on mechanical properties of the SWCNT solids, purified SWCNTs and raw soot were solidified by using the SPS method. The sintering temperature and pressure used for preparation of disk specimens are 1000°C and 120 MPa.

Figures 6 and 7 show the fractured specimens and stress-normalized displacement curves for both specimens, respectively. In the case of the raw soot solids, the main crack was formed at the center of the specimen that was subjected to the maximum biaxial stress and propagated to the outer region as shown in Fig. 6(a). The specimen was broken into four pieces, which demonstrated the brittle nature of the fracture. This observation corresponds to the deformation response as shown in Fig. 7. In contrast, the purified SWCNTs produced quasi-ductile solid structures. A fractured specimen is shown in Fig. 6(b), which is also illustrated schematically in Fig. 6(c). An indentation was formed on the specimen by the spherical puncher used for load application, and the main fracture initiated and propagated from a cone-shaped region at the edge of the indentation. A significant non-linear deformation response was observed for the SWCNT solids as shown in Fig. 7.

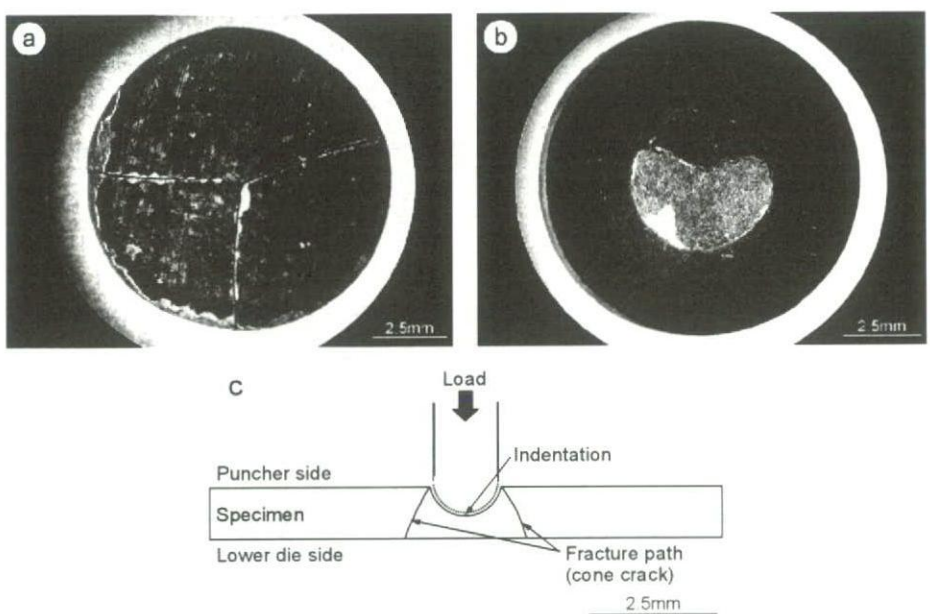

Fig. 6 Crack propagation of the (a) raw soot and (b) purified SWCNTs. Schematic illustration of the purified SWCNTs in also shown in (c).

The physical and mechanical properties for both specimens are shown in Table 2. The bulk density of the raw soot solids was found to be lager than that of the SWCNTs solids. This may be due to the presence of by-products such as metal particles, fullerenes and carbon materials in the raw soot solids. According to the density of raw soot solids, mass ratio of the metals contained in the raw soot is about 50 mass%. However, there was almost no difference in Young's modulus between the specimens. On the other hand, the work of fracture of the SWCNT solids was 12.4 times larger than that of the raw soot solids. The reason for the significant difference in the work of fracture may be due to the quasi-ductile fracture behavior of the SWCNT solids.

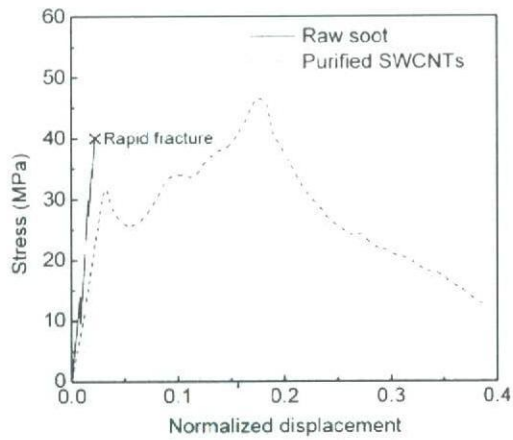

Fig. 7 Relation between stress and normalized displacement. (Processing condition: 1000°C, 120 MPa)

Table 2 Processing conditions and mechanical properties on the raw soot and purified SWCNTs prepared by spark plasma sintering.

Materials	Bulk density (Mg/m^3)	Young's modulus E_{SP} (GPa)	Work of fracture J_{SP} (N·mm)
Raw soot	1.90	0.76	1.4
Purified SWCNTs	1.55	0.66	17.3

3.2.2 Effects of Sintering Temperatures and Pressures

The effects of sintering temperatures and pressures on mechanical properties of the SWCNT solids were investigated. Here, the starting material used for preparation of solids is above-mentioned purified SWCNTs. Figure 8 shows the bulk density of the SWCNT solids as a function of sintering temperature. The theoretical density of individual SWCNTs has been calculated to be 1.36 Mg/m^3 [13][14], assuming the diameter of the SWCNTs to be 1.3 nm, and the distance between neighboring SWCNTs is determined by the van der Waals interaction. In the case of sintering pressure of 120 MPa, the density of the SWCNT solids tend to increase with the increasing sintering temperature and level off at about 1000°C. The saturation value is close to 1.6 Mg/m^3. On the other hand, the density of the SWCNT solids prepared at 40 MPa appears to at approximately 1200°C, and the saturation value is about 1.3 Mg/m^3. The reason for the density increase may be due to the structural change of the SWCNTs. It is well-known that the SPS technique is a pressure-assisted fast sintering method based on high-temperature plasma momentary generated in the gaps between powder materials by electrical discharge during on-off dc pulsing. It has been suggested that the dc pulse caused generate several effects such as spark plasma, spark impact, Joule

heating and an electrical diffusion [8]. Through these effects, it is expected that the density of the SWCNT solids give higher value than the theoretical density of individual SWCNTs.

The experimental measurements revealed that the mechanical properties of the SWCNT solids were dependent on the sintering temperature and pressure. Figure 9 gives typical load-displacement curves of the SWCNT solids determined from SP tests. Here, the sintering pressure used for preparation of SWCNT solids is 120 MPa. In all the specimens, cone-shaped fracture behavior was observed as shown in Figs. 6 (b) and (c). The nonlinear deformation response is observed up to the peak load followed by a long tail, for all the specimens. It is also seen that the initial slope and the peak load of the SWCNT solids increase with the increasing temperature. No clear change of the displacement at the maximum load was observed up to 1200°C, except for the SWCNT solids prepared at 1400°C. This phenomenon seems to correlate with the brittleness of the SWCNT solids prepared at 1400°C.

The Young's modulus E_{SP} of the SWCNT solids is plotted as a function of the sintering temperature in Fig. 10. It can be seen that the Young's modulus of the SWCNT solids increases with the increasing sintering temperature, in which the SWCNT solids prepared at 120 MPa gives higher value than that of SWCNT solids prepared at 40 MPa. However, it is unclear why the reduction in the Young's modulus occurs in the SWCNT solids prepared at a temperature of 1400°C and a pressure of 40 MPa.

Figure 11 shows the work of fracture of the SWCNT solids as a function of the processing temperature. It is seen that the variation of work of fracture with the processing conditions is approximately similar to that of the Young's modulus, except for the SWCNT solids prepared at a temperature of 1400°C and a pressure of 120 MPa. The reason for the drastic decrease may be due to the brittle fracture behavior as shown in Fig. 9.

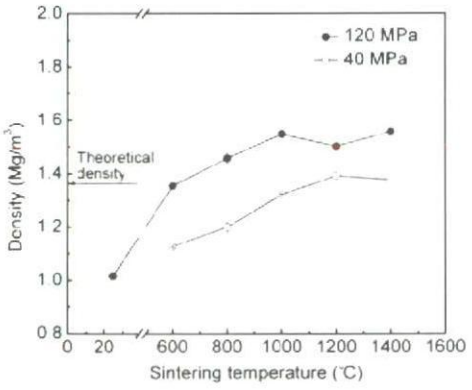

Fig. 8 Bulk densities of the SWCNT solids.

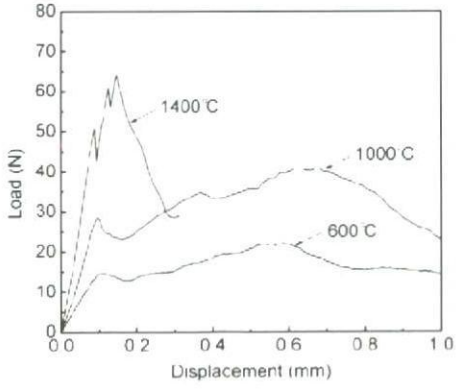

Fig. 9 Fracture behavior of the of the SWCNT solids.

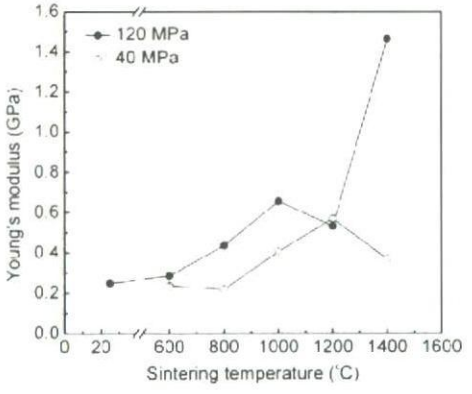

Fig. 10 Work of fracture of the SWCNT solids.

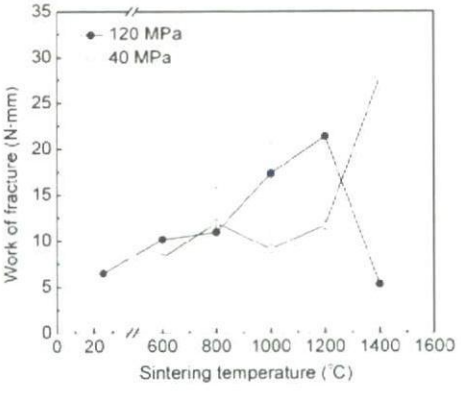

Fig. 11 Young's modulus of the SWCNT solids.

3.3 Microstructural Observation of the SWCNT Solid

The effects of sintering temperatures and pressures on nanostructure of the SWCNT solids were investigated. Figure 12 shows the Raman intensity ratio (I_G/I_D) for the SWCNT solids prepared under various processing conditions. Here, the I_G/I_D was normalized using the result of the SWCNT solids (I_G/I_D =70.0) consolidated by mechanical compaction only at room temperature and a pressure of 120 MPa. As shown in Fig. 12, the I_G/I_D of the SWCNT solids consolidated by mechanical compaction at room temperature was independent of the applied pressure. However, the I_G/I_D gradually decreased with increasing temperature and pressure, suggesting the transformation of SWCNTs into more stable structure. However, the Raman analysis provides no information about the structure of the SWCNT solids. Thus, we also carried out the microstructural observations of the SWCNT solids prepared under the various conditions.

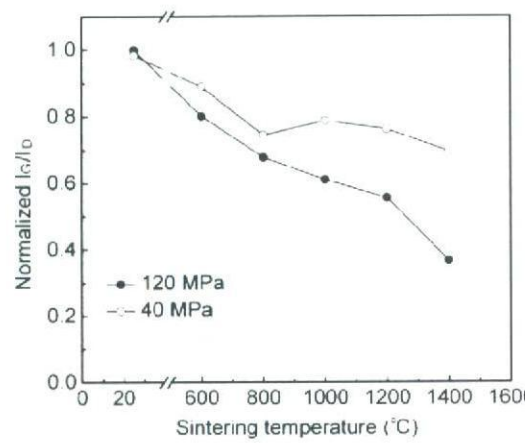

Fig. 12 Normalized IG/ID of the SWCNT solids as a function of sintering temperature.

Microstructural observations were carried out using SEM and TEM. Figure 13 shows a typical SEM image of fracture surface for the SWCNT solids prepared at a temperature of 1200°C and a pressure of 120 MPa. Extensive "pullout" of SWCNT bundles with approximately 3 μm in length was observed and the diameter of bundles was observed to decrease toward their tips. These experimental results indicate that the failure in the SWCNT solids prepared at lower sintering temperature occurred via sliding along the bundle surface or intra-bundles sliding between SWCNTs. The nonlinear deformation response of the SWCNT solids may be due to the pullout behavior of the bundles associated with the slippage of SWCNTs held by weak van der Waals interaction. Figures 14 and 15 show the typical TEM images of structure and fracture surface of the SWCNT solid prepared at a temperature of 600°C and a pressure of 120 MPa. It is seen that the bulk body provides a laminated structure of SWCNT bundles. As shown in Fig. 15, TEM image shows the SWCNT bundles contain 10~30 nanotubes extruding from the fracture surface. Detailed observation of the pullout bundles indicates that no breakage of SWCNTs occurred in the bundles. However, when the processing temperature was increased, the pulled out region was observed to decrease. As seen in Fig. 16, only a limited extent of pullout is observed in the SWCNT solid prepared at 1400°C. The pullout length of the bundles was obviously shorter, and the number of SWCNT bundles present was less than that of the SWCNT solids prepared at 600°C. It is noted that the outer surface of the bundles in the SWCNT solids prepared at 1400°C is much rougher than that of the ones prepared at 600°C. Namely, the SWCNT bundles in the high-temperature treated solids have irregular outer surface morphology with significant asperities, compared with the smooth outer surface in the